Optimization of CMOS-ISFET-Based Biomolecular Sensing: Analysis and Demonstration in DNA Detection

Guangyu Xu, *Member, IEEE*, Jeffrey Abbott, and Donhee Ham, *Senior Member, IEEE*

***Abstract*— Ion-sensitive field-effect transistors (ISFETs) have been used to detect a variety of biomolecules whose charges alter the current or threshold voltage of the transistor. ISFETs can be built into large-scale arrays by CMOS compatible technology, offering the promise of highly parallel, all-electrical biomolecule sensing in a true chip-scale construct. Although CMOS-ISFET-based biomolecule detection has been amply demonstrated, a comprehensive optimization study of its sensitivity based on the device design, which would aid the development of large-scale arrays, remains lacking. Here, we present a systematic optimization strategy for CMOS-ISFET-based biomolecule sensing, using real-time DNA hybridization detection as an example. We analytically show that biasing the ISFETs close to the threshold is optimal, whereas minimizing the channel-to-sensing area ratio is beneficial but with limited sensitivity enhancement due to the double-layer capacitance of the sensing area. We then experimentally confirm our strategy with 26 ISFETs of varying sizes and biases from two CMOS chips, which detect the same 200-nM target DNA with different hybridization signals. The measured data correlate well to the presented theory. Our results are generally applicable to detecting other types of biomolecules, and may help in developing large-scale arrays of electrical biomolecular sensors.**

***Index Terms*— Biomolecular sensing, CMOS, CMOS integrated circuits, DNA array, ion-sensitive field effect transistor (ISFET).**

I. Introduction

A WEALTH of research efforts has been dedicated to developing electrical biomolecular sensors, which respond to the biomolecular charges in the electrolytic solution and can enable real-time, label-free operation on the true chip-scale platform [1]–[4]. Among them, field-effect transistors (FETs) based on nanomaterials, such as semiconductor nanowires, carbon nanotubes, and graphene, have demonstrated high detection sensitivities in the subpicomolar range [5]–[7]. Another example is the ion-sensitive FET (ISFET); it was originally developed for pH sensing [8], [9] and has subsequently been applied for electronic detection of various types of biomolecules [10]. As the ISFETs can be implemented with CMOS technology, they can be readily built into large-scale arrays [11]–[13], and thus hold promise for highly parallel, all-electrical biomolecular sensing [14], [15].

One particularly well-suited example application of such parallelism of CMOS-ISFETs would be an all-electrical DNA microarray. Currently, the fluorescence-based optical DNA microarray is an important tool in molecular biology and molecular diagnostics [16] and achieves parallel operation with picomolar (pM) sensitivity [17], [18]. While CMOS-ISFETs have been used to detect DNA [9], [19]–[26], their development into a commercial array with performance comparable with the optical DNA array has yet to be achieved.

The development of such a large-scale CMOS-ISFET-based biomolecule—-DNA and beyond—-sensing array can benefit from systematic CMOS-ISFET design optimization studies. To date, researchers have investigated the dependencies of the CMOS-ISFET DNA detection sensitivity on probe DNA [21], electrochemistry [20], [27], and device geometry [19]. The geometry was also investigated in the context of ISFET pH sensing, where a larger sensing electrode area compared with the transistor channel was reported to achieve sensitivity beyond the Nernst equation [28]. Furthermore, optimizations on nanowire FET sensors, while outside of our discussion strictly on CMOS-ISFETs here, have accounted for the capacitance of the double-layer [29] and subthreshold biasing [30], [31] and their effects on FET charge sensitivity. While these studies are useful, it would be even more beneficial if a systematic optimization strategy in CMOS-ISFET biomolecule sensing is explicitly studied, putting various effects together.

We here build upon the prior studies and incorporate all aspects of bias and geometry to carry out a systematic study of the optimization of the CMOS ISFET's inherent charge sensitivity. We analytically show that the real-time detection signal can be enhanced by biasing the ISFET at the near-threshold region together with the device having a small area ratio

Manuscript received March 30, 2016; accepted June 17, 2016. Date of publication July 9, 2016; date of current version July 21, 2016. This work was supported in part by the National Science Foundation under Contract DMR-1231319, and in part by the Catalyst Foundation of Valhalla, NY. The review of this paper was arranged by Editor C. K. Sarkar. *(Guangyu Xu and Jeffrey Abbott contributed equally to this work.)*

G. Xu was with the School of Engineering and Applied Sciences, Harvard University, Cambridge, MA 02138 USA. He is now with the Department of Electrical and Computer Engineering, University of Massachusetts, Amherst, MA 01003 USA (e-mail: guangyux@umass.edu).

J. Abbott and D. Ham are with the School of Engineering and Applied Sciences, Harvard University, Cambridge, MA 02138 USA (e-mail: jabbott@seas.harvard.edu; donhee@seas.harvard.edu).

Color versions of one or more of the figures in this paper are available online at http://ieeexplore.ieee.org.

Digital Object Identifier 10.1109/TED.2016.2582845

0018-9383 © 2016 IEEE. Personal use is permitted, but republication/redistribution requires IEEE permission.
See http://www.ieee.org/publications_standards/publications/rights/index.html for more information.

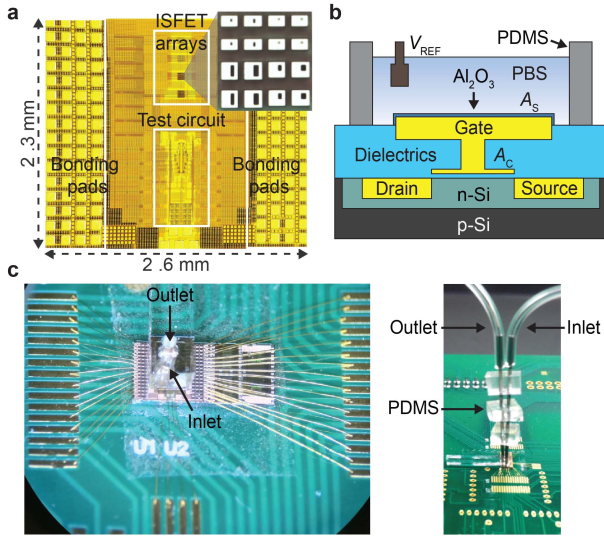

Fig. 1. CMOS-ISFET array and experimental setup. (a) Optical micrograph of a fabricated CMOS chip with four 4 × 4 ISFET arrays. Inset: the sensing areas of a 4 × 4 ISFET array after postprocessing. (b) Cross-sectional illustration of an individual ISFET site. (c) Top down (left) and side view (right) images of a packaged CMOS chip with a microfluidic channel on top. The entire device is attached and wire bonded to a printed circuit board.

between the transistor channel and the sensing electrode, while the sensitivity limit arises from the double-layer capacitance of the sensing electrode in solution. We then experimentally confirm our co-optimization strategy with 26 CMOS-ISFETs of varying sizes and biases, from two separate CMOS chips fabricated in 0.18-μm technology; they detect the same 200-nM target DNA hybridization with different sensitivities, with good correlation to the presented theory. The results of this performance optimization study, which are applicable not only to DNA but also other biomolecules with inherent charges, may help develop a variety of large-scale CMOS-ISFET biosensor arrays.

II. Materials and Methods

A. Fabrication of ISFET Arrays and Microfluidics

We fabricate floating-gate ISFET arrays in 0.18-μm CMOS technology through a silicon foundry (using 3.3 V devices with a gate oxide thickness of $t_{ox} = 70$ Å), and postprocess the silicon chips in-house to expose the top metal (Al) of the floating gates (Fig. 1). Each chip contains four identical ISFET arrays with each array consisting of 4×4 p-type ISFETs [Fig. 1(a)]. We use two chips for this study, and DNA detection experiments are performed with the third array from the chip edge for each chip. The floating gate of each ISFET [24], [26], shown in Fig. 1(b) has an upper side facing electrolyte with a larger sensing area A_S (width: W_S; length: L_S), and a bottom side facing the FET channel with a smaller channel area A_C, where its corresponding width W and length L are those of the FET channel. The 16 ISFETs in the third array of each chip are designed with varying A_S and A_C values, with channel length L ranging from the short-channel process minimum of 0.3 μm to a long-channel maximum of 1.5 μm (Table I).

TABLE I
Device Geometries of the 4 × 4 CMOS-ISFET Array

Device	L (μm)	W (μm)	L_S (μm)	W_S (μm)	A_C/A_S
1, 5	0.3	4.0	11.86	8.06	1/80
2, 6	0.3	6.0	12.86	8.06	1/58
3, 7	0.5	1.2	11.93	8.06	1/160
4, 8	0.35	1.2	11.90	8.06	1/230
9, 13	1.0	16.0	12.17	12.9	1/9.8
10, 14	1.5	16.0	13.13	12.9	1/7.1
11, 15	1.0	8.0	12.25	11.7	1/18
12, 16	1.5	8.0	12.23	11.7	1/12

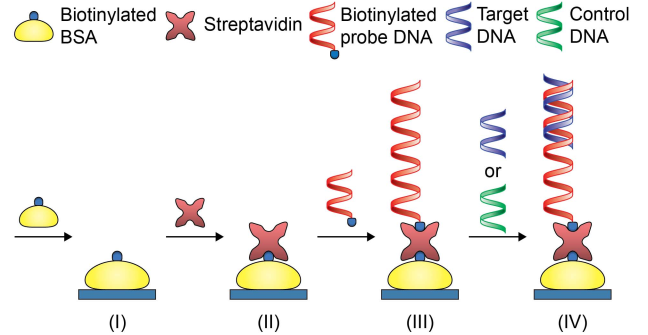

Fig. 2. Steps in DNA experiments, including BSA-streptavidin surface functionalization (I and II), probe DNA immobilization (III), and hybridization or control experiments (IV).

To expose the top metal of the floating gate, we use reactive-ion etching (RIE). Before RIE, the contact metal pads and the backside of the chip are covered by photoresist to prevent the RIE plasma from breaking down the ISFET gates, though some fixed charge is still accumulated on the floating gate causing variations in the threshold voltage among the different ISFETs. After RIE, a native Al_2O_3 layer (∼5-nm thick) naturally forms on the exposed metal. This Al_2O_3 layer acts as a sensing area that anchors probe DNA to which the target DNA is hybridized [19].

A microfluidic channel (length × width × height = 1.5 mm × 1 mm × 60 μm) is then fabricated on top of the chip [Fig. 1(c)]. This facilitates robust controllable delivery and removal of electrolyte, DNA molecules, and surface functionalization materials. The microfluidic channel has inlet and outlet tubings; an Ag/AgCl wire inserted through the outlet tubing acts as a reference electrode in the electrolyte, and provides reference voltage V_{REF}. The silicon chip and microfluidic channel are assembled on a printed circuit board with bonding wires connecting the ISFET-array chip and the printed circuit [Fig. 1(c)].

B. Surface Functionalization

We functionalize the ISFET sensing areas so that they can anchor the probe DNA molecules (Fig. 2) [2], [5], [32]. We first treat the chip surface with biotinylated bovine-serum-albumin (BSA) for ca. 2 h. After DI water rinsing, we subsequently expose the chip surface to streptavidin for ca. 1.5 h, during which streptavidin binds to biotinylated BSA.

These streptavidin molecules provide the sites for biotinylated probe DNA molecules to bind (Section II-C). These surface treatment steps are executed while floating the reference electrode voltage V_{REF} and keeping the source and drain voltages of each ISFET, V_S and V_D, at 0 V.

C. Probe DNA Immobilization and Electrical Detection of Target DNA Hybridization

After the surface functionalization, we rinse the chip with 0.005 × phosphate buffered saline (PBS). 200 nM of single-stranded probe DNAs are then introduced in DI water for immobilization onto the ISFET sensing areas. After a 1-h wait, itinerant probe DNA is washed with 0.005 × PBS. Subsequently, in 0.005 × PBS, we record the source-to-drain current I_{SD}, of each ISFET in the 4 × 4 ISFET array in real time; the sources of the 16 ISFETs are connected together, while their drain nodes connect to an external 16:1 multiplexer; each I_{SD} is first amplified by a low-noise current preamplifier (SR570) and recorded by a multimeter (Agilent 34411A) at every ~20 s. When each current stabilizes into less than a 1% difference within a 30-min window, 200-nM single-stranded target DNA, whose sequence is complementary to a 20-base partial sequence of the probe DNA, is introduced in DI water. After a 1-h wait for hybridization, itinerant target DNA is removed by 0.005 × PBS rinsing. We then measure I_{SD} in 0.005 × PBS until its stabilization. In all of these electrical measurements, the source–drain voltage V_{SD} of each ISFET is kept at 0.5 V. This is a largely arbitrary value to ensure that no ISFET enters the linear region for various gate voltages that differ from device to device to test our optimization theory.

The target DNA hybridization can be detected by observing the increase in the stabilized value of posthybridization-phase I_{SD} from that of prehybridization-phase I_{SD}, because DNA is negatively charged and our ISFETs are p-type. Throughout the prehybridization and posthybridization phases [hybridization phase], 0.005 × PBS [target DNA solutions] are added once every 14 min to avoid bubble formation. With 0.005 × PBS, the Debye length λ_D is ~10.7 nm [3], [33], sufficient for our ISFETs to sense the hybridized DNA charges.

D. DNA Sequence

The sequence of probe DNA is 5'-biotin-TGGCGACGGCA GGAGGCTGAGGTAGTAGTTTGTACAGTTA-Cy3-3', where the underlined 20-base segment is complementary to the shorter target DNA, whose sequence is 5'-Cy5-CTGTACAAACTACTACCTCA-3'. This sequence is complementary to the 20-base segment (underlined) of 22-mer miRNA let7g, 5'-UGAGGUAGUAGUUUGUACAGUU-3', which is widely believed to mediate tumor suppression in human cancer [34], [35]. The control DNA used in lieu of the target DNA in control experiments is 5'-TGAGGTAGTAGATTGTATAGTT-3'. We choose a shorter target/control DNA sequence complementary to the 3' end of a longer probe DNA due to empirical observations that hybridizing target DNAs close to the 5' end may be less efficient. We attribute this to the positive charge of the streptavidin (pI = 5.6 [33]) in 0.005 × PBS electrostatically attracting the 5' end of the probe DNAs, possibly preventing those nucleotides from being accessible for hybridization.

E. Analyte Details

Details of the various analytes mentioned in the foregoing are as follows: 1) 1-mg/mL biotinylated-BSA in 18.2-MΩ · cm deionized water; 2) 0.2-mg/mL streptavidin in 1 × TE; 3) probe DNA, target DNA, and control DNA in 18.2-MΩ · cm deionized water; 4) and diluted 0.005 × PBS from 1 × PBS by 18.2-MΩ · cm deionized water. Here, 1 × PBS is the standard solution with 137-mM NaCl and 1 × TE is the standard solution with 10-mM Tris and 1-mM ethylenediaminetetraacetic acid. The biotinylated-BSA and streptavidin are from Sigma Aldrich; DNA is from Integrated DNA Technologies.

III. Results and Discussion

A. Bias-Geometry Co-Optimization Theory of CMOS-ISFETS

We now describe the ISFET optimization strategy in the context of real-time DNA detection, while the following analysis applies to sensing other biomolecules with inherent charges in electrolyte. Let Q_{H} be the total *effective* surface charge brought by the hybridized target DNA onto the sensing area of a p-ISFET ($Q_{\mathrm{H}} < 0$). Q_{H} is not in general the total charge $Q_{\mathrm{H,total}}$ of the entire target DNA molecules hybridized onto the ISFET, but it is the *effective* surface charge that affects the ISFET conductance; this distinction is needed because, for example, a fraction of $Q_{\mathrm{H,total}}$ may be too distant from the sensing area to affect the ISFET conductance. Q_{H} will increase the ISFET channel current from I_{SD} to $I_{\mathrm{SD}} + \Delta I_{\mathrm{SD}}$.

We seek to quantify the normalized current change $\Delta I_{\mathrm{SD}}/I_{\mathrm{SD}}$ as a function of the effective surface charge density $q'_{\mathrm{H}} = Q_{\mathrm{H}}/A_{\mathrm{S}}$ ($q'_{\mathrm{H}} < 0$) with the ISFET bias and geometry as parameters, so that we can co-optimize the ISFET's *intrinsic* charge sensitivity with its geometry and biasing. This is opposed to maximizing Q_{H} (or $q'_{\mathrm{H}} = Q_{\mathrm{H}}/A_{\mathrm{S}}$) for a given $Q_{\mathrm{H,total}}$ (or $Q_{H,\mathrm{total}}/A_{\mathrm{S}}$), which is highly influenced by electrochemistry and probe DNA optimization. Although these optimizations are important for the overall DNA detection sensitivity, they are outside the scope of this paper, which is focused on the intrinsic ISFET sensitivity. It is important to note, however, that the bias point of the floating gate can influence Q_{H} within the established electric field interface between the sensing gate and the electrolyte [7], [31], [36]–[38], and should be considered if optimizing the system as a whole. In a more general context, these discussions with Q_{H} can represent any effective biomolecular charge in solution, so long as the charge is affecting the ISFET conductance.

$Q_{\mathrm{H}} = q'_{\mathrm{H}} \cdot A_{\mathrm{S}}$ induces a negative voltage change of ΔV_{X} at the aluminum oxide surface, at the V_{X} node in Fig. 3(a), where $\Delta V_{\mathrm{X}} = Q_{\mathrm{H}}/C_{\mathrm{eq}}$ and C_{eq} is the equivalent small signal capacitance between node V_{X} and small signal ground. C_{eq} is calculated as the aluminum oxide double-layer capacitance C_{DBL} in parallel with the series combination of the aluminum oxide to gate capacitance C_{Al2O3} and total gate capacitance $C_{\mathrm{G}} = C_{\mathrm{GS}} + C_{\mathrm{GD}}$ (C_{GD}: gate–drain capacitance;

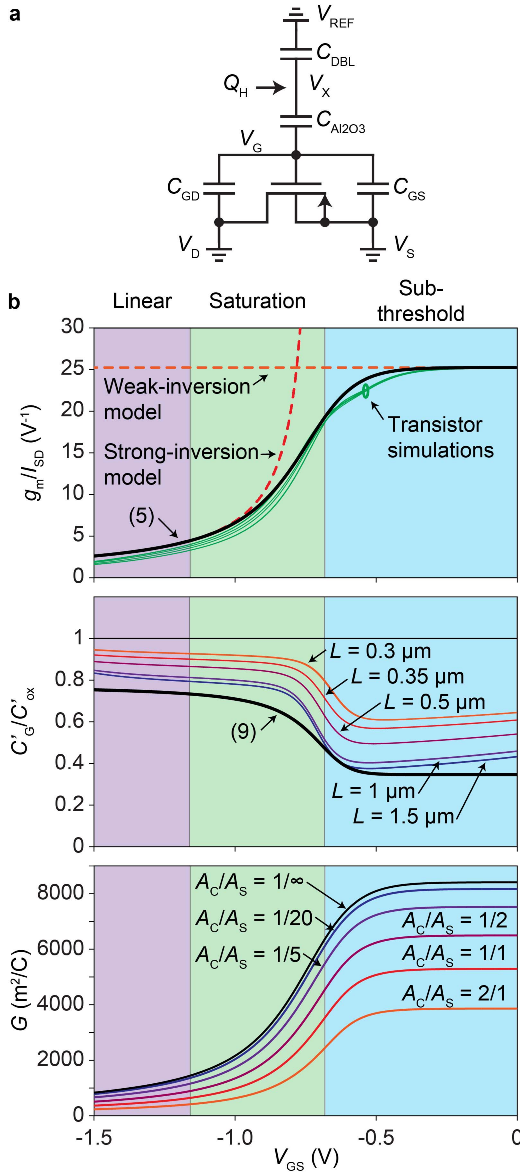

Fig. 3. Bias-geometry dependence of the G factor. (a) Small signal circuit model of the p-ISFET in solution. (b) Top: bias dependence of g_m/I_{SD} with varying $|V_{GS}|$. Transistor simulations (green lines) for all eight W/L ratios used with $V_{SD} = 0.5$ V are included in addition to the curve calculated from (5) (black line) and the weak-inversion and strong-inversion model approximations, (7) and (8) (dashed lines). Middle: simulated (nonblack lines) and calculated according to (9) (black line), C'_G/C'_{ox} with varying $|V_{GS}|$ for all the eight W/L ratios used for the ISFETs. Bottom: G with varying $|V_{GS}|$ calculated from (4), (5), and (9), for various A_C/A_S values. For the calculations, $V_{TH} = -0.7$ V, $n = 1.53$, $C'_{DBL} = 3$ mF/m^2, $C'_{ox} = 5.1$ mF/m^2.

C_{GS}: gate–source capacitance, in which we include the gate-body capacitance with the body tied to the source). We express these capacitances in terms of their corresponding per-unit-area capacitance densities multiplied by the relevant areas: $C_{DBL} = C'_{DBL} \cdot A_S$, $C_{Al2O3} = C'_{Al2O3} \cdot A_S$, and $C_G = C'_G \cdot A_C$. As the native aluminum oxide thickness is small (~5 nm) and the sensing area A_S is large in comparison with the MOSFET channel area A_C, C_{Al2O3} (>1 pF) is significantly larger than C_G (~10 fF) and ΔV_X is approximately equal to the corresponding change ΔV_G in the floating gate metal voltage V_G.

Taking all the above together, we relate q'_H and ΔV_G as follows:

$$\Delta V_X = \frac{Q_H}{\left(\frac{1}{C_{Al2O3}} + \frac{1}{C_{GS}+C_{GD}}\right)^{-1} + C_{DBL}} \approx \Delta V_G \approx \frac{q'_H A_S}{C'_G A_C + C'_{DBL} A_S}. \quad (1)$$

This negative ΔV_G will cause a positive ΔI_{SD} in the p-ISFET, where $\Delta I_{SD} = -g_m \cdot \Delta V_G$ in a small signal model with g_m (A/V) being the transconductance ($g_m = \mathrm{d}I_{SD}/\mathrm{d}V_{SG}$). Then the normalized ISFET channel current change is expressed as a function of q'_H as follows:

$$\frac{\Delta I_{SD}}{I_{SD}} = -\frac{g_m}{I_{SD}} \cdot \frac{A_S}{C'_G A_C + C'_{DBL} A_S} \times q'_H. \quad (2)$$

This is the sought-after expression that captures the intrinsic charge sensitivity of the ISFET, which may be rewritten as

$$\frac{\Delta I_{SD}}{I_{SD}} = -G q'_H \quad (3)$$

with G (m^2/C) defined as

$$G = \frac{g_m}{I_{SD}} \cdot \frac{1}{\frac{A_C}{A_S} C'_G + C'_{DBL}}. \quad (4)$$

This G is the figure of merit that represents the intrinsic charge sensitivity of the ISFET; to enhance the ISFET's intrinsic charge sensitivity, we should increase G by altering the ISFET gate biasing V_G that affects g_m, I_{SD}, and C'_G and by altering the geometric parameters A_C and A_S. Below, we examine the bias and geometry dependence of G by using an approximate long-channel formula that provides analytical guides and design insights, and also by complementing it with more accurate simulations that take into account the detailed device effects [e.g., short-channel effects, as our ISFETs come with submicron as well as micron channel lengths for geometric variations (Table I)].

As we increase $|V_{GS}|$ from zero, the ISFET's channel inverts, transitioning from weak- to moderate- and eventually strong-inversion. With the experimentally used V_{SD} being 0.5 V and V_{TH} denoting the threshold voltage (negative for p-ISFETs), during this increasing inversion, while $|V_{GS}| < |V_{TH}|$ we define the ISFET to be in the subthreshold region of operation, and once $|V_{GS}| > |V_{TH}|$, the device enters saturation (with $|V_{SD}| > |V_{GS} - V_{TH}|$) and eventual linear region (after $|V_{SD}| < |V_{GS} - V_{TH}|$). Using a long-channel expression for I_{SD} that captures the weak- and strong-inversion behaviors altogether, g_m/I_{SD} can be expressed smoothly as [39], [40]

$$\frac{g_m}{I_{SD}} = \frac{\xi}{n\varphi_t(1+\xi)\ln(1+\xi)} \quad (5)$$

with

$$\xi = e^{\frac{-(V_{GS}-V_{TH})}{2n\varphi_t}} \quad (6)$$

where $\phi_t = k_B T/e$ and n is a process-dependent unitless number commonly between 1 and 1.5. In the weak inversion extreme ($V_{GS} > V_{TH}$, $|V_{GS} - V_{TH}| \gg n\phi_t$)

well into the subthreshold regime and in the strong inversion extreme ($V_{GS} < V_{TH}$, $|V_{GS} - V_{TH}| \gg n\phi_t$) well into the saturation regime, (5) collapses to the following well-established relations, respectively:

$$\frac{g_m}{I_{SD}} \approx \frac{1}{n\varphi_t} \tag{7}$$

$$\frac{g_m}{I_{SD}} \approx \frac{2}{-(V_{GS} - V_{TH})}. \tag{8}$$

The gate capacitance per unit area C'_G normalized to the gate oxide capacitance per unit area C'_{ox} can also be calculated smoothly across the saturation and subthreshold regions [39]

$$\frac{C'_G}{C'_{ox}} = \frac{2\Lambda}{n + 3n\Lambda + n\sqrt{1+4\Lambda}} + \frac{n-1}{n} \tag{9}$$

with

$$\Lambda = \ln^2(1+\xi). \tag{10}$$

g_m/I_{SD} and C'_G/C'_{ox} of (5) and (9) are plotted as functions of V_{GS} in Fig. 3(b) (top and middle), respectively, with $V_{TH} = -0.7$ V and $n = 1.53$ an approximate fit to the process parameters; the extrapolation of (5) and (9) into the less important linear region in Fig. 3(b) with no reference to the used $V_{SD} = 0.5$ V is done for the sake of brevity; this approximation produces correct qualitative behaviors, as seen with simulations shortly. As shown in these calculations, with decreasing $|V_{GS}|$ and with the ISFET making transition from saturation to subthreshold regime, g_m/I_{SD} is increased to a plateaued maximum value [41] and C'_G/C'_{ox} is decreased to a plateaued minimum value as the inverted channel charge is reduced.

These general patterns are confirmed with simulations more accurate than (5) and (9). Briefly, sources are applied to the SPICE models provided by the silicon foundry, with the gate voltage swept $V_{SD} = 0.5$ V and the I_{SD}, g_m, and small signal, low frequency ac gate current measured. The g_m/I_{SD} is then directly calculated, while C'_G/C'_{ox} is calculated from the ac current and the process parameters for C'_{ox}. Fig. 3(b) (top) shows that simulated g_m/I_{SD} largely agrees with (5), varying very little among the wide range of W/L ratios used in our work, including both short and long channel devices ($L = 0.3$–1.5 μm). Fig. 3(b) (middle) shows that the overall dependency of simulated C'_G/C'_{ox} with varying $|V_{GS}|$ is also similar to the calculated result. However, the simulated C'_G/C'_{ox} shows a dependency on the ISFET channel length, which is absent in (9) and thus unseen in the calculated figure, and is also larger than the calculation; this is largely due to the extrinsic fringing capacitance of the gate to source/drain terminals prominent in shorter channel devices, which (9) does not take into account. For more accurate equation-based calculation of C'_G/C'_{ox}, this extrinsic capacitance can be included using appropriate process parameters [39].

Combining these bias effects in connection with the expression of G in (4), for a given floating gate geometry with fixed A_s and A_c, decreasing $|V_{GS}|$ into the subthreshold region offers a higher G; for g_m/I_{SD} in the numerator of (4), it increases toward the maximum into the subthreshold region and C'_G in its denominator finds near minimum values in the subthreshold region. However, decreasing $|V_{GS}|$ deep into the subthreshold regime close to 0 V has limited benefits, because g_m/I_{SD} already hits the maximum plateau before $|V_{GS}|$ is brought down to 0 V and C'_G hits a minimum or tends to go back up slightly as shown with simulation. Furthermore, and importantly, with $|V_{GS}|$ decreased deep into the subthreshold regime, not only does I_{SD} decrease exponentially to make its measurement significantly more difficult, but the 1/f noise of the pMOS transistor also saturates or even increases [42], [43]. Therefore, biasing the transistor around the border between the saturation and the subthreshold offers not only an optimal biasing that best compromises between magnitude of current and highest charge sensitivity, but also the highest signal-to-noise ratio in pMOS transistors.

G also depends on the floating gate geometry, specifically A_C/A_S, as seen in (4). To increase G for a given biasing, one should reduce A_C/A_S—by decreasing A_C and increasing A_S—which is a factor in the C'_G term in the denominator of (4). However, as the C'_G term grows smaller with the A_C/A_S reduction, the denominator becomes ultimately dominated by the C'_{DBL} term, beyond which the A_C/A_S reduction will not be effective in further increasing G. Fig. 3(b) (bottom) shows this dependence by plotting Gversus $|V_{GS}|$, using (5) and (9) for various A_C/A_S values. For these plots, we use $C'_{DBL} \sim 3$ mF/m^2 (we estimate this double-layer capacitance by assuming that it consists of a capacitance of the stern layer with ~1 Debye length, 10-nm, thickness, and a dielectric constant of 6 in series with a capacitance of the diffusion layer with ~4 Debye lengths, 40 nm, and dielectric constant of 30 [44], [45]) and $C'_{ox} = 5.1$ mF/m^2 ($t_{ox} = 70$ Å) for the 0.18-μm process. These plots show that G can be increased not indefinitely but by up to a factor of ~2, when A_C/A_S is reduced from its nominal value of 1 to 0; the reduction of A_C/A_S below 1/20 is not effective due to the finite C'_{DBL}. Further increase in G can therefore be achieved by reducing C'_{DBL} by lowering the solution concentration [3], [33].

Altering A_C/A_S or C'_{DBL} will not only change the intrinsic small signal sensitivity of the ISFET device, but it will also change the dc potential of the floating gate [Fig. 3(a)]. From a large signal analysis, the dc potential of V_G is determined by a capacitive voltage divider between the electrolyte potential and the source/drain terminals: by altering the transistor channel area, sensing electrode area, or C'_{DBL}, the dc transfer function from the reference electrode to V_G will be affected in addition to the strength of the electric field between the aluminium oxide and electrolyte [7], [31], [36]–[38]. As a consequence, ISFETs with different geometries will require different reference voltages to be biased near the threshold.

B. DNA Detection Experiments

To verify our optimization theory, we perform DNA detection experiments with the ISFET arrays. In this section, we present the detection measurements across the arrays, and in the next section, we analyze the measurements and compare them with the theory.

During the measurements, both geometry and bias are varied among different ISFETs for the purpose of achieving a spread

of G values to compare with their hybridization signals. Geometry is directly varied by designing the ISFET arrays with A_C/A_S values ranging from 1/6.5 to 1/230 (Table I). Bias variation, however, is indirectly accomplished by fixing a common reference electrode voltage V_{REF} in the shared electrolyte for a given chip during the entire real-time experiment, such that all ISFETs are approximately biased near the threshold (i.e., $V_{GS} \sim V_{TH} \sim -0.7$ V). As V_{TH} varies around the nominal threshold voltage of ~ -0.7 V from device to device due to process variations and due importantly to the variations in the fixed charge that can accumulate on the floating gate, and as each device has a different transfer function from V_{REF} to V_G due to the ranging A_C/A_S, each device is in fact biased with varying effective V_{GS}–V_{TH} values. In addition, we adjust V_{REF} from -0.15 to -0.1 V for the two chips used in the experiments to provide a larger range of bias conditions, which adds to the spread of G values. Overall, from our measurements, we estimate a range of 0.43 V for V_{GS}–V_{TH} across the arrays with biasing in both the subthreshold and saturation regions.

Fig. 4(a) (top) shows a measured real-time trace of I_{SD} (back calculated from the SR570-amplified voltage signal) from an ISFET with $W/L = 6\ \mu$m/0.25 μm and $A_C/A_S = 1/58$, before, during, and after the hybridization phase with 200-nM target DNA, where $V_{REF} = -0.1$ V was used for the array containing this ISFET. Before hybridization, I_{SD} is stabilized to 15.8 μA. During hybridization, I_{SD} goes up due to the relatively large amount of target DNAs in solution gating the ISFET and due also to a change of the ion concentration from 0.005 × PBS solution prior to and DI water during hybridization. After the hybridization phase, I_{SD} relaxes back to another stable value of 18.1 μA. Overall, the hybridized target DNA causes a net increase in the stabilized value of I_{SD} [3], [19]. In contrast, the control experiment with 200 nM control DNA—whose sequence is not complementary to probe DNA—does not show as appreciable a current change before and after hybridization [Fig. 4(a) (bottom)]. We note that the control and hybridization experiments are performed sequentially on the same ISFET array with the same bias; to this end, a 45-min treatment with 90 °C deionized water is used to remove any residual control DNA after the control experiment, and the chip is then refunctionalized with biotinylated BSA and streptavidin, and probe DNA sequentially reintroduced, yielding a similar amount of immobilized probe DNA before the hybridization experiment [7]. In addition, the periodic spikes in the current trace result from the addition of 0.005 × PBS [target/control DNAs] at every 14 min during the prehybridization and posthybridization phases [hybridization phase] to prevent bubble formation.

The 200-nM hybridization results from all ISFETs from two separate arrays (two separate chips) are shown in Fig. 4(b), along with the signals from the control experiment performed in one of the two arrays ($V_{REF} = -0.15$ V for Chip I target, $V_{REF} = -0.1$ V for Chip II target and control). Independent of the bias condition or device geometry, a total of 26 out of 32 ISFETs show their 200-nM hybridization signals well separated from the 200-nM control signals. Device 12, Chip I,

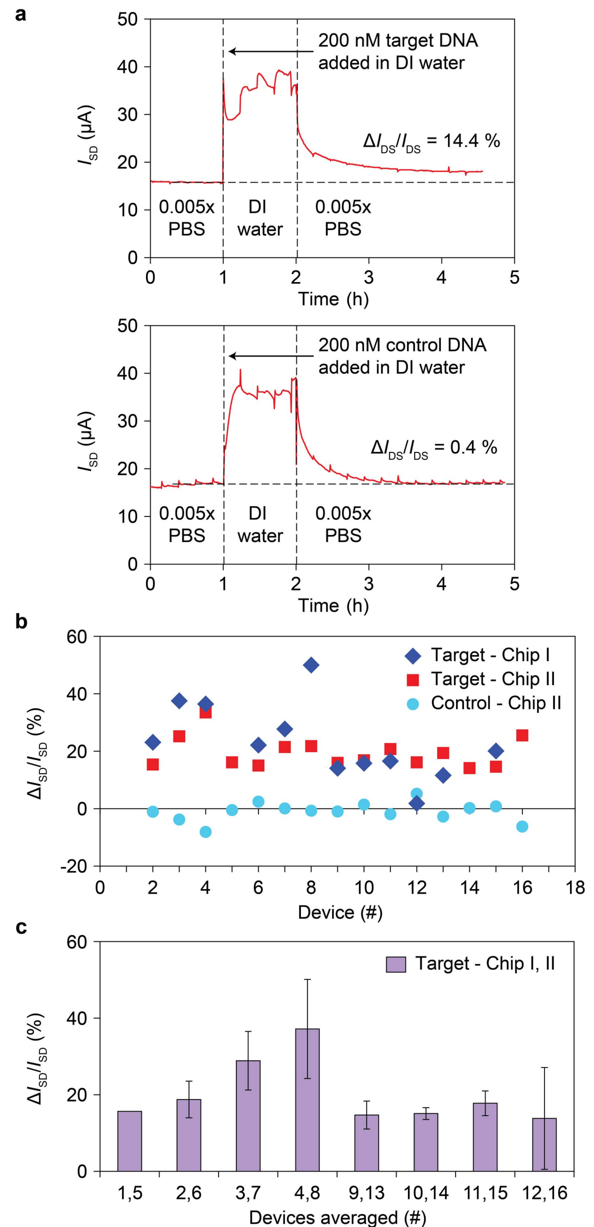

Fig. 4. DNA detection experiments. (a) 200-nM hybridization data (top) and 200-nM control data (bottom) from device 6 on Chip II, in which the ISFET is biased at $V_{REF} = -0.10$ V, $V_S = 0.5$ V, and $V_D = 0$ V. The 1-h DNA hybridization [control] step is marked as the region between the two vertical dotted lines. (b) 200-nM target hybridization and control signals ($\Delta I_{SD}/I_{SD}$) for each ISFET site. (c) Target hybridization signal averages and standard deviations (error bars) for Chip I and II devices with the same geometries.

which is not counted toward the 26 working devices, but is still shown in Fig. 4(b), shows no change of current from before to after hybridization. The five devices omitted from Fig. 4(b) are either degraded after postprocessing or their source-to-drain current is too low to be accurately measured. The tendency for the control experiments to shift negative might result from the negatively charged control DNAs partially binding to the far 3' end of the probe DNAs, thus electrostatically pushing the probe DNA away from the ISFET sensing area at the 5' end and causing a decrease in the current.

Averaging the hybridization results from devices with identical geometries from both Chip I and Chip II, shown with

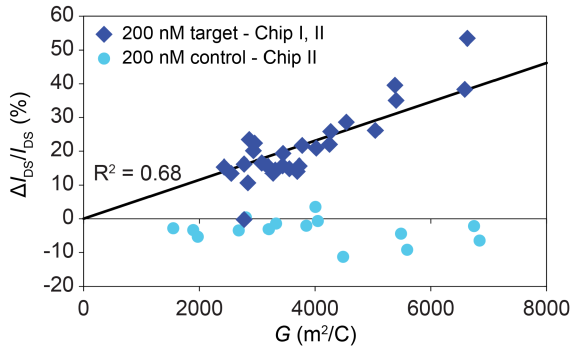

Fig. 5. Quantifications of the DNA hybridization and control signals ($\Delta I_{SD}/I_{SD}$). G-dependence of 200-nM hybridization signals for Chips I and II and 200-nM control signals for Chip II.

calculated standard deviations in Fig. 4(c), reveals a qualitatively increasing trend for A_C/A_S (see Table I). The largest A_C/A_S of 1/230 for the geometry of devices 4 and 8 yields a ~2 × larger signal than that of the long channel devices with an A_C/A_S of ~1/10. Importantly, these data with good yield across the arrays allow us to next quantitatively verify the presented theory.

C. Quantifications of the DNA Detection Signal

We verify our optimization theory by correlating the measured $\Delta I_{SD}/I_{SD}$ and the G factor we extract from the measured I_{SD} (Fig. 5). Since we cannot directly measure V_{GS}–V_{TH} of the ISFET as we have access to the gate only through the electrolyte, for each ISFET, we use the 30-min measured and averaged prehybridization I_{SD} value at the steady state in conjunction with simulated $I_{SD} - g_m/I_{SD}$ and $I_{SD} - C'_G/C'_{ox}$ curves to extract G. As seen in Fig. 5, the measured $\Delta I_{SD}/I_{SD}$increases with the extracted G, with a linear fit $R^2 = 0.68$ for the wide range of G, which confirms our optimization theory (we expect a similar q'_H across different ISFETs as we perform the same surface treatment for each device). From the data, for a larger G, created by a reduction of A_C/A_S and biasing closer to or in subthreshold, a larger hybridization signal is measured. A smaller G, on the other hand, has a much reduced hybridization signal, due to a larger A_C/A_S and biasing further away from the subthreshold in the saturation region. Furthermore, the hybridization data are well separated from those in the control experiment, in which we obtain a similar range of G values among ISFETs; this further demonstrates the cogency of our study.

IV. Conclusion

In sum, we performed a systematic study of optimization of CMOS-ISFETs to improve their inherent charge sensitivity. The real-time charge detection signal can be enhanced by biasing the ISFET near threshold, by reducing its channel-to-sensing area ratio, and by minimizing the double-layer capacitance of the sensing electrode. This study is verified by 26 CMOS-ISFETs of varying sizes and biases, which detect the same 200-nM target DNA with different hybridization signals in real-time current monitoring. To lower the limit of detection for future works, properly optimized device geometries and biasing could be combined with increased probe concentration and electrolyte Debye lengths. This optimization study may be useful for the implementation of a large-scale CMOS-ISFET array for a variety of biomolecular sensing applications.

References

[1] B. R. Dorvel *et al.*, "Silicon nanowires with high-*k* hafnium oxide dielectrics for sensitive detection of small nucleic acid oligomers," *ACS Nano*, vol. 6, no. 7, pp. 6150–6164, 2012.
[2] C. Kataoka-Hamai and Y. Miyahara, "Label-free detection of DNA by field-effect devices," *IEEE Sensors J.*, vol. 11, no. 12, pp. 3153–3160, Dec. 2011.
[3] A. Poghossian, A. Cherstvy, S. Ingebrandt, A. Offenhäusser, and M. J. Schöning, "Possibilities and limitations of label-free detection of DNA hybridization with field-effect-based devices," *Sens. Actuators B, Chem.*, vols. 111–112, pp. 470–480, Nov. 2005.
[4] A. Star, E. Tu, J. Niemann, J.-C. P. Gabriel, C. S. Joiner, and C. Valcke, "Label-free detection of DNA hybridization using carbon nanotube network field-effect transistors," *Proc. Nat. Acad. Sci. USA*, vol. 103, no. 4, pp. 921–926, 2006.
[5] J.-I. Hahm and C. M. Lieber, "Direct ultrasensitive electrical detection of DNA and DNA sequence variations using nanowire nanosensors," *Nano Lett.*, vol. 4, no. 1, pp. 51–54, 2004.
[6] S. Sorgenfrei *et al.*, "Label-free single-molecule detection of DNA-hybridization kinetics with a carbon nanotube field-effect transistor," *Nature Nanotechnol.*, vol. 6, no. 2, pp. 126–132, 2011.
[7] G. Xu *et al.*, "Electrophoretic and field-effect graphene for all-electrical DNA array technology," *Nature Commun.*, vol. 5, Sep. 2014, Art. no. 4866.
[8] P. Bergveld, "Development of an ion-sensitive solid-state device for neurophysiological measurements," *IEEE Trans. Biomed. Eng.*, vol. BME-17, no. 1, pp. 70–71, Jan. 1970.
[9] P. Bergveld, "Thirty years of ISFETOLOGY: What happened in the past 30 years and what may happen in the next 30 years," *Sens. Actuators B, Chem.*, vol. 88, no. 1, pp. 1–20, 2003.
[10] M. Yuqing, G. Jianguo, and C. Jianrong, "Ion sensitive field effect transducer-based biosensors," *Biotechnol. Adv.*, vol. 21, no. 6, pp. 527–534, 2003.
[11] A. Hierlemann, U. Frey, S. Hafizovic, and F. Heer, "Growing cells atop microelectronic chips: Interfacing electrogenic cells *in vitro* with CMOS-based microelectrode arrays," *Proc. IEEE*, vol. 99, no. 2, pp. 252–284, Feb. 2011.
[12] B. Premanode, N. Silawan, W. P. Chan, and C. Toumazou, "A composite ISFET readout circuit employing current feedback," *Sens. Actuators B, Chem.*, vol. 127, no. 2, pp. 486–490, 2007.
[13] T. C. W. Yeow, M. R. Haskard, D. E. Mulcahy, H. I. Seo, and D. H. Kwon, "A very large integrated pH-ISFET sensor array chip compatible with standard CMOS processes," *Sens. Actuators B, Chem.*, vol. 44, nos. 1–3, pp. 434–440, Oct. 1997.
[14] C.-S. Lee, S. K. Kim, and M. Kim, "Ion-sensitive field-effect transistor for biological sensing," *Sensors*, vol. 9, no. 9, pp. 7111–7131, 2009.
[15] B. He, T. J. Morrow, and C. D. Keating, "Nanowire sensors for multiplexed detection of biomolecules," *Current Opinion Chem. Biol.*, vol. 12, no. 5, pp. 522–528, 2008.
[16] A. Sassolas, B. D. Leca-Bouvier, and L. J. Blum, "DNA biosensors and microarrays," *Chem. Rev.*, vol. 108, no. 1, pp. 109–139, 2008.
[17] A. L. Ghindilis *et al.*, "CombiMatrix oligonucleotide arrays: Genotyping and gene expression assays employing electrochemical detection," *Biosensors Bioelectron.*, vol. 22, nos. 9–10, pp. 1853–1860, 2007.
[18] Y. Li, Y. T. H. Cu, and D. Luo, "Multiplexed detection of pathogen DNA with DNA-based fluorescence nanobarcodes," *Nature Biotechnol.*, vol. 23, no. 7, pp. 885–889, 2005.
[19] M. Barbaro, A. Bonfiglio, L. Raffo, A. Alessandrini, P. Facci, and I. Barák, "Fully electronic DNA hybridization detection by a standard CMOS biochip," *Sens. Actuators B, Chem.*, vol. 118, nos. 1–2, pp. 41–46, 2006.
[20] C. Gentil, G. Philippin, and U. Bockelmann, "Signal enhancement in electronic detection of DNA hybridization," *Phys. Rev. E-Statist. Nonlinear, Soft Matter Phys.*, vol. 75, no. 1, pp. 011926-1–011926-4, 2007.

[21] T. Uno, H. Tabata, and T. Kawai, "Peptide–nucleic acid-modified ion-sensitive field-effect transistor-based biosensor for direct detection of DNA hybridization," *Anal. Chem.*, vol. 79, no. 1, pp. 52–59, 2007.

[22] F. Uslu, S. Ingebrandt, D. Mayer, S. Böcker-Meffert, M. Odenthal, and A. Offenhäusser, "Labelfree fully electronic nucleic acid detection system based on a field-effect transistor device," *Biosensors Bioelectron.*, vol. 19, no. 12, pp. 1723–1731, 2004.

[23] M. J. Milgrew, P. A. Hammond, and D. R. S. Cumming, "The development of scalable sensor arrays using standard CMOS technology," *Sens. Actuators B, Chem.*, vol. 103, nos. 1–2, pp. 37–42, 2004.

[24] J.-K. Shin, D.-S. Kim, H.-J. Park, and G. Lim, "Detection of DNA and protein molecules using an FET-type biosensor with gold as a gate metal," *Electroanalysis*, vol. 16, no. 22, pp. 1912–1918, 2004.

[25] B. C. Jacquot, N. Muñoz, D. W. Branch, and E. C. Kan, "Non-faradaic electrochemical detection of protein interactions by integrated neuromorphic CMOS sensors," *Biosensors Bioelectron.*, vol. 23, no. 10, pp. 1503–1511, 2008.

[26] T. Sakata and Y. Miyahara, "DNA sequencing based on intrinsic molecular charges," *Angew. Chem. Int. Ed.*, vol. 45, no. 14, pp. 2225–2228, 2006.

[27] K. Jayant, K. Auluck, S. Rodriguez, Y. Cao, and E. C. Kan, "Programmable ion-sensitive transistor interfaces. III. Design considerations, signal generation, and sensitivity enhancement," *Phys. Rev. E-Statist. Nonlinear, Soft Matter Phys.*, vol. 89, no. 5, pp. 052817-1–052817-12, 2014.

[28] K. B. Parizi, A. J. Yeh, A. S. Y. Poon, and H. S. P. Wong, "Exceeding Nernst limit (59 mV/pH): CMOS-based pH sensor for autonomous applications," in *Proc. Int. Electron Devices Meeting*, 2012, pp. 24.7.1–24.7.4.

[29] K. Shoorideh and C. O. Chui, "On the origin of enhanced sensitivity in nanoscale FET-based biosensors," *Proc. Nat. Acad. Sci. USA*, vol. 111, no. 14, pp. 5111–5116, Mar. 2014.

[30] X. P. A. Gao, G. Zheng, and C. M. Lieber, "Subthreshold regime has the optimal sensitivity for nanowire FET biosensors," *Nano Lett.*, vol. 10, no. 2, pp. 547–552, 2010.

[31] K. Shoorideh and C. O. Chui, "Optimization of the sensitivity of FET-based biosensors via biasing and surface charge engineering," *IEEE Trans. Electron Devices*, vol. 59, no. 11, pp. 3104–3110, Nov. 2012.

[32] G. M. Credo *et al.*, "Label-free electrical detection of pyrophosphate generated from DNA polymerase reactions on field-effect devices," *Analyst*, vol. 137, no. 6, pp. 1351–1362, Feb. 2012.

[33] E. Stern, R. Wagner, F. J. Sigworth, R. Breaker, T. M. Fahmy, and M. A. Reed, "Importance of the debye screening length on nanowire field effect transistor sensors," *Nano Lett.*, vol. 7, no. 11, pp. 3405–3409, Nov. 2007.

[34] K. Ohshima *et al.*, "Let-7 MicroRNA family is selectively secreted into the extracellular environment via exosomes in a metastatic gastric cancer cell line," *PLoS ONE*, vol. 5, no. 10, p. e13247, Oct. 2010.

[35] M. S. Kumar *et al.*, "Suppression of non-small cell lung tumor development by the let-7 microRNA family," *Proc. Nat. Acad. Sci. USA*, vol. 105, no. 10, pp. 3903–3908, Mar. 2008.

[36] K. Jayant *et al.*, "Programmable ion-sensitive transistor interfaces. I. Electrochemical gating," *Phys. Rev. E-Statist. Nonlinear, Soft Matter Phys.*, vol. 88, no. 1, p. 012801, 2013.

[37] K. Jayant *et al.*, "Programmable ion-sensitive transistor interfaces. II. Biomolecular sensing and manipulation," *Phys. Rev. E-Stat. Nonlinear, Soft Matter Phys.*, vol. 88, no. 1, p. 012802, 2013.

[38] Y. Liu and R. W. Dutton, "Effects of charge screening and surface properties on signal transduction in field effect nanowire biosensors," *J. Appl. Phys.*, vol. 106, no. 1, p. 014701, 2009.

[39] Y. Tsividis, *Operation and Modeling of the MOS Transistor*, 2nd ed. New York, NY, USA: Oxford Univ. Press, 1999.

[40] Y. Tsividis, K. Suyama, and K. Vavelidis, "Simple 'reconciliation' MOSFET model valid in all regions," *Electron. Lett.*, vol. 31, no. 6, pp. 506–508, 1995.

[41] F. Silveira, D. Flandre, and P. G. A. Jespers, "A g_m/I_D based methodology for the design of CMOS analog circuits and its application to the synthesis of a silicon-on-insulator micropower OTA," *IEEE J. Solid-State Circuits*, vol. 31, no. 9, pp. 1314–1319, Sep. 1996.

[42] J. Chang, A. A. Abidi, and C. R. Viswanathan, "Flicker noise in CMOS transistors from subthreshold to strong inversion at various temperatures," *IEEE Trans. Electron Devices*, vol. 41, no. 11, pp. 1965–1971, Nov. 1994.

[43] Y. Nemirovsky, I. Brouk, and C. G. Jakobson, "$1/f$ noise in CMOS transistors for analog applications," *IEEE Trans. Electron Devices*, vol. 48, no. 5, pp. 921–927, May 2001.

[44] A. J. Bard and L. R. Faulkner, *Electrochemical Methods—Fundamentals and Applications*, 2nd ed. Hoboken, NJ, USA: Wiley, 2004.

[45] E. Gileadi, E. Kirowa-Eisner, and J. Penciner, *Interfacial Electrochemistry: An Experimental Approach*. Reading, MA, USA: Addison-Wesley, 1975.

Guangyu Xu (M'11) received the B.S. and M.S. degrees in fundamental sciences and electrical engineering from Tsinghua University, Beijing, China, in 2003 and 2006, respectively, and the Ph.D. degree in electrical engineering from the University of California, Los Angeles, CA, USA, in 2011.

He has been an Assistant Professor of Electrical and Computer Engineering with the University of Massachusetts Amherst, MA, USA, since 2016. His current research interests include building integrated molecule detection and multiplexed cell imaging tools, aiming to provide new capabilities for next-generation personal health.

Jeffrey Abbott received the B.S./M.S. degrees in electrical engineering from the Rochester Institute of Technology, Rochester, NY, USA, in 2011. He is currently pursuing the Ph.D. degree in electrical engineering with the Harvard School of Engineering and Applied Sciences, Cambridge, MA, USA.

His current research interests include analog integrated circuits, applications of nanotechnology to neuroscience, and CMOS biosensors.

Donhee Ham (SM'12) received the B.S. degree in physics from Seoul National University, Seoul, South Korea, in 1996. He received the Ph.D. degree in electrical engineering from the California Institute of Technology, Pasadena, CA, USA, in 2002.

He is the Gordon McKay Professor of Applied Physics and Electrical Engineering with Harvard University. His current research interests include quantum and low-dimensional materials, applications of nanotechnology to neuroscience, RF and analog integrated circuits, and biomolecular spectroscopic techniques.